UNIVERSITY OF BIRMINGHAM

University of Birmingham
Research at Birmingham

Efficient solar-driven CO2-to-fuel conversion via Ni/MgAlO$_x$ @SiO$_2$ nanocomposites at low temperature

Liu, Xianglei; Ling, Yueyue; Sun, Chen; Shi, Hang; Zheng, Hangbin; Song, Chao; Gao, Ke; Dang, Chunzhuo; Sun, Nan; Xuan, Yimin; Ding, Yulong

Link to publication on Research at Birmingham portal

Article

Efficient solar-driven CO_2-to-fuel conversion via Ni/MgAlO$_x$@SiO$_2$ nanocomposites at low temperature

Xianglei Liu [a], Yueyue Ling [a], Chen Sun [a], Hang Shi [a], Hangbin Zheng [a], Chao Song [a], Ke Gao [a], Chunzhuo Dang [a], Nan Sun [a], Yimin Xuan [a,*], Yulong Ding [b]

[a] School of Energy and Power Engineering, Nanjing University of Aeronautics and Astronautics, Nanjing 210016, China
[b] Birmingham Centre for Energy Storage, School of Chemical Engineering, University of Birmingham, Birmingham B15 2TT, United Kingdom

ARTICLE INFO

ABSTRACT

Solar-driven CO_2-to-fuel conversion assisted by another major greenhouse gas CH_4 is promising to concurrently tackle energy shortage and global warming problems. However, current techniques still suffer from drawbacks of low efficiency, poor stability, and low selectivity. Here, a novel nanocomposite composed of interconnected Ni/MgAlO$_x$ nanoflakes grown on SiO$_2$ particles with excellent spatial confinement of active sites is proposed for direct solar-driven CO_2-to-fuel conversion. An ultrahigh light-to-fuel efficiency up to 35.7%, high production rates of H_2 (136.6 mmol min^{-1}g^{-1}) and CO (148.2 mmol min^{-1}g^{-1}), excellent selectivity (H_2/CO ratio of 0.92), and good stability are reported simultaneously. These outstanding performances are attributed to strong metal-support interactions, improved CO_2 absorption and activation, and decreased apparent activation energy under direct light illumination. MgAlO$_x$@SiO$_2$ support helps to lower the activation energy of CH* oxidation to CHO* and improve the dissociation of CH_4 to CH_3* as confirmed by DFT calculations. Moreover, the lattice oxygen of MgAlO$_x$ participates in the reaction and contributes to the removal of carbon deposition. This work provides promising routes for the conversion of greenhouse gasses into industrially valuable syngas with high efficiency, high selectivity, and benign sustainability.

1. Introduction

The progress of modern industrialization is accompanied by the massive consumption of fossil fuels, particularly oil and coal, leading to the shortage of these unrenewable resources and emission of large amounts of carbon dioxide (CO_2) [1–3]. Recently, CO_2 concentrations in the atmosphere have exceeded 415 ppm, which is about 50% higher than pre-industrial levels. Induced by massive CO_2 emissions, global warming has seriously threatened the balance of natural ecosystems [4]. Similar to CO_2, global emissions of methane (CH_4), which is another major greenhouse gas [5], have increased by nearly 10% over the past two decades, and its atmospheric concentration has set a new record of 1.875 ppm [6,7]. Given the warming power of CH_4 is 80 times as high as that of CO_2, CH_4 is believed as the second most prevalent greenhouse gas from human activities. Subsequently, how to deal with these greenhouse gasses is an urgent problem to be solved [6,8,9]. Conversion of two major greenhouse gasses into value-added syngas ($CH_4 + CO_2 \rightarrow 2CO + 2H_2$, $\Delta H_{298K} = 247$ kJ/mol), which is also called CO_2 reduction by methane (CRM), is considered

to be one of the most promising approaches to achieve sustainable development [10].

Different metal catalysts have been employed as active components for CRM reaction, such as Fe, Co, Ni, Ru, Rh and so on. Noble metals have high catalytic activity, but their high costs and limited availability prevent their practical large-scale applications. Ni has become the most widely used catalyst for its comparably high activity and low cost, but it suffers from deactivation due to carbon deposition and sintering of Ni nanoparticles (NPs). Carbon deposition mainly comes from the two side reactions, i.e., of methane dissociation ($CH_4 \rightarrow C + 2H_2$, $\Delta H_{298K} = 75$ kJ/mol) and carbon monoxide disproportionation ($2CO \rightarrow C + CO_2$, $\Delta H = -172$ kJ/mol) [11,12]. Reducing the size of NPs has been demonstrated to limit carbon nucleation and growth, but nanoparticles tend to aggregate into large particles at high reaction temperature, leading to poor stability. Confining metal NPs inside mesoporous materials, such as porous shells and matrixes, has been reported to be effective in mitigating sintering [13,14]. Nevertheless, some active sites are inevitably covered and inhibited to interact with reaction gasses, leading to decreasing CRM activities. Therefore,

---

* Corresponding author.
E-mail address: ymxuan@nuaa.edu.cn (Y. Xuan).
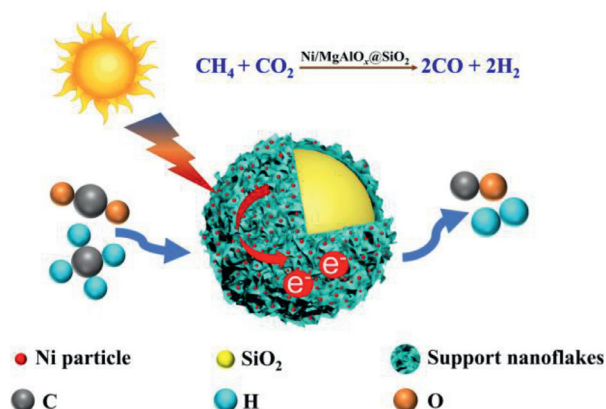
Scheme 1. Schematic illustration of the solar-driven CRM process on Ni/MgAlO$_x$@SiO$_2$ catalyst.

enabling metal NPs to possess small sizes, high activity and high stability simultaneously is still a daunting challenge.

Another concern of CRM is its highly endothermic nature, so that massive thermal energy is needed to drive reactions. Emerging solar-driven CRM not only supplies thermal energy required in a low carbon way, but also can store solar energy in the form of important feedstocks or fuels [15–18], thus serving as a promising candidate to tackle global energy and climate change problems simultaneously. The key parameter determining whether solar-driven CRM can be widely deployed is high solar-to-fuel efficiency. People have devoted extensive efforts to enhancing solar-to-fuel efficiency. For example, many different catalysts have been developed to improve the catalytic activity and efficiency [19–26], and the highest solar-to-fuel efficiency reported under mild conditions is only 33.8%. Further enhancing solar-to-fuel efficiency over 35% is still a desire.

Here, we proposed interconnected Ni/MgAlO$_x$ nanoflakes grown on SiO$_2$ particles to achieve highly efficient solar-driven CO$_2$-to-fuel conversion (shown in Scheme 1). An extremely large light-to-fuel efficiency of 35.7% and very high fuel production rates of H$_2$ and CO (136.6 and 148.2 mmol min^{-1}g^{-1}) are achieved under focused illumination. Excellent spatial confinement of active sites, strong metal-support interactions, improved CO$_2$ absorption and activation, and decreased apparent activation energy of C* and CH* species under direct light illumination are considered the main mechanisms, as confirmed by both experimental measurements and DFT calculations. In addition, the lattice oxygen of MgAlO$_x$ in the nanocomposite takes part in the reaction which helps to decrease carbon species as will be discussed later.

2. Material and methods

2.1. Synthesis of catalysts

Mg(NO$_3$)$_2$·6H$_2$O (0.164 g, 0.64 mmol), Al(NO$_3$)$_3$·9H$_2$O (0.135 g, 0.36 mmol), SiO$_2$ (0.12 g) and CO(NH$_2$)$_2$ (2.7 g) were dispersed in 8 ml deionized water. 9 ml C$_2$H$_5$OH and 8 ml Ni(NO$_3$)$_2$·6H$_2$O (0.1 M) were then added. After stirring for five hours, the solution was dropped in a Teflon-lined stainless steel autoclave heating for 36 h at 190 °C. The resulting suspension was centrifuged and washed three times with ethanol, and then the product was dried overnight. Finally, the powders were reduced under 10% H$_2$/Ar at 700 °C for 3 h. The reduced sample was labeled as Ni/Mg$_{1.78}$AlO$_x$@SiO$_2$. The samples with the Mg/Al molar ratio of 0.67, 1.22 and 2.03 were prepared after following similar procedures. Correspondingly, 0.26 g Mg(NO$_3$)$_2$·6H$_2$O (or 0.37 g Al(NO$_3$)$_3$·9H$_2$O), 0.12 g SiO$_2$ and 2.7 g CO(NH$_2$)$_2$ were employed to obtain Ni/MgO@SiO$_2$ or Ni/Al$_2$O$_3$@SiO$_2$. The procedures were the same as Ni/Mg$_{1.78}$AlO$_x$@SiO$_2$. Ni@SiO$_2$ sample was synthesized via the same procedures except that Mg(NO$_3$)$_2$·6H$_2$O was not added.

2.2. CO$_2$-to-fuel conversion tests

The CO$_2$-to-fuel conversion was conducted in a homemade reactor with a quartz window. We put 0.019 g of catalysts in the reactor for every test. A stream of CH$_4$/CO$_2$/N$_2$ (43.2%/43.2%/13.6%) was continuously fed to the reactor at 104.2 ml min^{-1}. A 300 W Xe lamp was used as the light source without using any other heating devices. The irradiation power focused on samples was measured by a laser power meter, which was calibrated by AM 1.5 global solar light with a standard Si solar cell. The power of the focused UV–Vis-IR illumination is measured to be 12.0 W. Since the spot diameter is 6 mm, the irradiation density reaches 424.6 kW m^{-2}.

The light-to-fuel efficiency(η) is defined as follows:

$$\eta = \frac{\left(r_{H_2} \times \Delta_c H^0_{H_2} + r_{CO} \times \Delta_c H^0_{CO} - r_{CH_4} \times \Delta_c H^0_{CH_4} \right)}{P_{\text{irradiation}}}$$

where r_{H_2} and r_{CO} are the molar production rate of H$_2$ and CO, respectively, and r_{CH_4} is the reaction rate of CH$_4 \cdot \Delta_c H^0_{CO_2}$, $\Delta_c H^0_{CO}$ and $\Delta_c H^0_{CH_4}$ are the standard heat of combustion ($\Delta_c H^0$, 298.15 K) of H$_2$, CO and CH$_4$ fuel, respectively (note: CO$_2$ is not a fuel, so $\Delta_c H^0_{CO_2}$ of CO$_2$ is 0), and $P_{\text{irradiation}}$ is the irradiation power focused on the reactor.

3. Results and discussion

3.1. Catalyst characterizations

The structure and components of prepared catalysts were investigated by X-ray diffraction (XRD). MgO and Al$_2$O$_3$ are in the form of Mg-phyllosilicate Mg$_3$Si$_4$O$_{10}$(OH)$_2$ (PDF 29–1493) and Al-phyllosilicate Al$_2$Si$_2$O$_5$(OH)$_4$ (PDF 14–0164), respectively, both of which are at the same peak (2θ = 42.6°) in Fig. 1a. When MgO is combined with Al$_2$O$_3$, it exists in the form of MgAl$_2$Si$_2$O$_6$(OH)$_4$ (PDF 35–0489). This fully shows that there is a strong interaction between magnesium oxide, aluminum oxide and silicon oxide [27]. All the samples show three diffraction peaks at 2θ of 44.5°, 51.8° and 76.3°, which correspond to the (111), (200) and (220) crystal plane of Ni [28,29], respectively. As shown in Fig. 1b, there is one more peak at 26.619° belonging to MgAl$_2$Si$_2$O$_6$(OH)$_4$ in Ni/Mg$_{1.78}$AlO$_x$@SiO$_2$, suggesting that different Mg/Al molar ratios affect the combination of MgO, Al$_2$O$_3$ and SiO$_2$. XRD results confirm that Mg^{2+} and Al^{3+} exist in the form of phyllosilicates instead of bulk MgO and Al$_2$O$_3$, illustrating strong interactions between Mg-Al phyllosilicates and the support SiO$_2$.

The surface morphology and element mapping analysis of the catalysts were investigated by a transmission electron microscope (TEM) and scanning electron microscopy (SEM). TEM images (Fig. 1c) show that the structure of the Ni/Mg$_{1.78}$AlO$_x$@SiO$_2$ catalyst is similar to a sphere. Internal pores are beneficial to enhance the surface area and limit the agglomeration of metal particles. According to N$_2$ adsorption/desorption measurements (Fig. S1), the surface area of Ni/Mg$_{1.78}$AlO$_x$@SiO$_2$ is 112.5 cm^2 (Table 1). Although this value is not the largest among different samples, the average particle size of Ni nanoparticles before the reaction is the smallest with a value of only 8.65 nm (Fig. S3). Small Ni nanoparticles can suppress coking since carbon nanofibers are more difficult to nucleate, not to mention subsequent growth [28,30]. Ni nanoparticles are shown as bright dots in Fig. 1d, and their interplanar distance is 0.208 nm as shown in Fig. 1e [31]. Due to the addition of excessive urea, the solution is alkaline, so SiO$_2$ particles partially dissolve and form Mg-Al phyllosilicate with Mg^{2+} and Al^{3+} (Fig. 1f). MgAl-phyllosilicate crystal lattice effectively suppressed the growth and migration of Ni nanoparticles. Through the corresponding element mapping of Ni, Mg, Al, Si, O (Fig. 1g), all the elements are dispersed uniformly on the surface of the carrier. Good dispersion and small size of Ni nanoparticles help to achieve both good catalytic activity and durability.
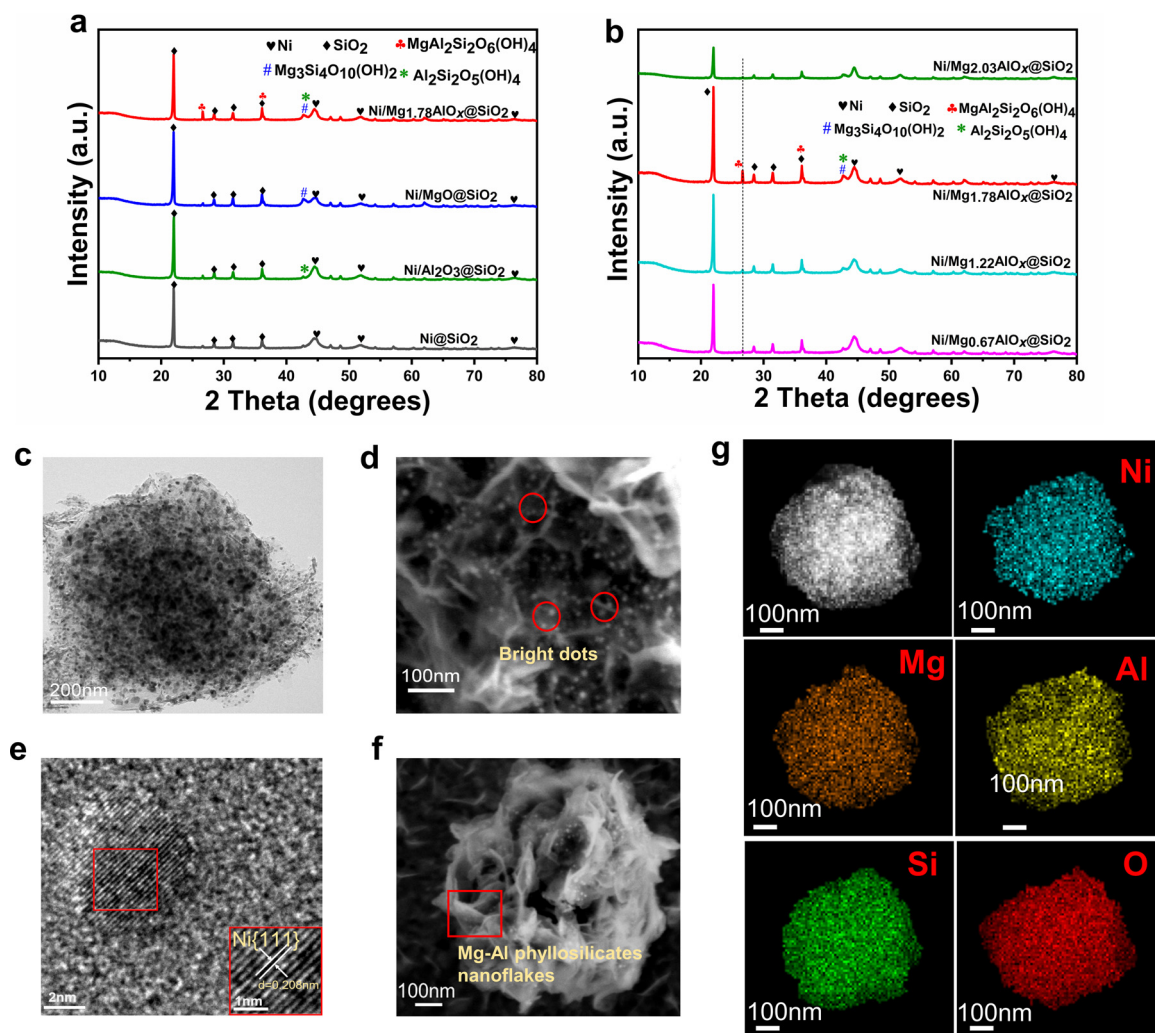
Fig. 1. Crystal structure and morphology of catalysts. (a) XRD patterns of Ni/Mg$_{1.78}$AlO$_x$@SiO$_2$, Ni/MgO@SiO$_2$, Ni/Al$_2$O$_3$@SiO$_2$, Ni@SiO$_2$. (b) XRD patterns of Ni/Mg$_{2.03}$AlO$_x$@SiO$_2$, Ni/Mg$_{1.22}$AlO$_x$@SiO$_2$ and Ni/Mg$_{0.67}$AlO$_x$@SiO$_2$. (c) TEM, (d) Enlarged SEM, (e) HRTEM and (f) SEM images of the Ni/Mg$_{1.78}$AlO$_x$@SiO$_2$. (g) High-angle annular dark-field scanning TEM (HAADF-TEM) image of Ni/Mg$_{1.78}$AlO$_x$@SiO$_2$ and element mapping.

Table 1
Element composition and structural properties of different samples.

Sample	Metal elemental composition[a] Ni Mg Al (wt%) (wt%) (wt%)			S_{BET} (m^2/g)[b]	V_p (cm^3/g)[c]	D_{SEM} (nm)[d]
Ni@SiO$_2$	27.8	–	–	153.9	0.31	16.55
Ni/MgO@SiO$_2$	22.6	11.1	–	124.5	0.27	12.72
Ni/Mg$_{2.03}$AlO$_x$@SiO$_2$	21.3	6.8	5.1	88.2	0.39	–
Ni/Mg$_{1.78}$AlO$_x$@SiO$_2$	21.5	6.6	4.8	112.5	0.54	8.65
Ni/Mg$_{1.22}$AlO$_x$@SiO$_2$	22.0	5.8	6.2	106.5	0.57	–
Ni/Mg$_{0.67}$AlO$_x$@SiO$_2$	23.6	4.3	7.9	88.0	0.44	–
Ni/Al$_2$O$_3$@SiO$_2$	23.5	–	10.6	64.5	0.45	11.87

[a] Metal elemental composition was detected through an Inductively Coupled Plasma-Optical Emission Spectroscopy (ICP-OES).
[b] BET specific surface areas.
[c] Average pore volumes were determined by BJH method.
[d] Average particle size of metal Ni NPs was detected via SEM.

It is well known that the metal-support interaction is an important factor affecting CRM performances [32]. Here, H$_2$-temperature programmed reduction (H$_2$-TPR) experiments of the samples were conducted to check their metal-support interactions (Fig. 2a). There is a broad peak between 400 °C and 600 °C for each catalyst, which is corresponding to the medium interaction between Ni species and the support [29,33]. It is worth noting that catalysts containing Mg-Al supports have a narrow reduction peak over 600 °C, which indicates that a small part of NiO has strong interactions with the support. An additional peak centered on 732.4 °C is found for Ni/Mg$_{1.78}$AlO$_x$@SiO$_2$, which suggests even stronger metal-support interaction [13]. A higher reduction temperature means the sintering resistance of metal nanoparticles is better.
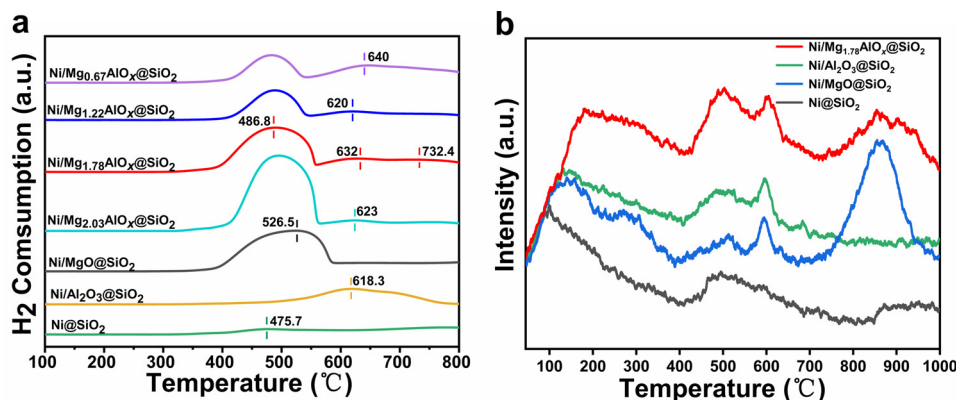
Fig. 2. Characterization of catalysts. (a) H_2-TPR profiles of different catalysts. (b) CO_2-TPD profiles of Ni/Mg$_{1.78}$AlO$_x$@SiO$_2$, Ni/Al$_2$O$_3$@SiO$_2$, Ni/MgO@SiO2, Ni@SiO$_2$.

That also indicates the combination of magnesium and aluminum effectively increases metal-support interactions, which contributes to the small sizes of Ni nanoparticles (Fig. S3).

The basic sites of catalyst surfaces have a great influence on the adsorption and dissociation of CO_2 [34,35]. Strong alkalinity can effectively promote CO_2 adsorption and dissociation [36]. As shown in Fig. 2b, samples exhibited a low temperature desorption peak between 100 °C and 200 °C which is attributed to weak basic sites in catalysts. The desorption peak between 400 °C and 500 °C is attributed to strong basic sites. Interestingly, Ni/MgO@SiO$_2$ has a strong desorption peak around 860 °C, suggesting it has strong alkalinity at high temperature. Therefore, Ni/Mg$_{1.78}$AlO$_x$@SiO$_2$ displays the most basic sites that contributed to strong carbon dioxide adsorption capacity [37]. CO_2 is the only oxygen-containing reactant in CRM, and generated active oxygen from CO_2 dissociation can interact with carbon species to avoid continuous deposition of carbon on the catalyst surface ($CO_2 + C \rightarrow 2CO$). The adsorbed CO_2 reacts with newly formed carbon species, which plays a significant role in eliminating carbon deposition. Thus, it is expected to achieve low carbon deposition and good stability for those catalysts possessing more basic sites, such as Ni/Mg$_{1.78}$AlO$_x$@SiO$_2$.

3.2. Ultrahigh solar-to-fuel conversion efficiency

The photothermocatalytic activity of CRM was conducted in a homemade reactor with a quartz window (Fig. S5). Upon the focused UV–vis-IR irradiation, the surface temperature of the samples reached the equilibrium temperature quickly (Fig. S6). Gas chromatography was employed to detect both reactants and products. As shown in Fig. 3a, b, for Ni@SiO$_2$, the production rates of H_2 (r_{H_2}) and CO (r_{CO}) are 45.1 mmol min^{-1}g^{-1} and 62.4 mmol min^{-1}g^{-1}, respectively. The r_{H_2} and r_{CO} of Ni/Al$_2$O$_3$@SiO$_2$ increase to 92.8 mmol min^{-1}g^{-1} and 115.4 mmol min^{-1}g^{-1}, and the r_{H_2} and r_{CO} of Ni/MgO@SiO$_2$ become 89.7 mmol min^{-1}g^{-1} and 109.6 mmol min^{-1}g^{-1} respectively. It is obvious that magnesium aluminum silicate as the support increases both activity and stability significantly. For Ni/Mg$_{0.67}$AlO$_x$@SiO$_2$, r_{H_2} and r_{CO} are 120.8 mmol min^{-1}g^{-1} and 138.4 mmol min^{-1}g^{-1}, respectively. When the Mg/Al molar ratio is 1.22, its r_{H_2} and r_{CO} increase further to 115.6 mmol min^{-1}g^{-1} and 135.5 mmol min^{-1}g^{-1}, respectively. Especially, Ni/Mg$_{1.78}$AlO$_x$@SiO$_2$ exhibits the best catalytic performance. Its r_{H_2} and r_{CO} are 136.6 mmol min^{-1}g^{-1} and 148.2 mmol min^{-1}g^{-1}, respectively. Reaction rates of CH$_4$(r_{CH_4}) and CO_2 (r_{CO_2}) are 75.0 mmol min^{-1}g^{-1} and 81.2 mmol min^{-1}g^{-1}, respectively. In addition, r_{H_2} is slightly lower than r_{CO} in all experiments, so that H_2/CO ratio is less than 1 (Table 2), which is attributed to the existence of the reverse water-gas shift reaction ($CO_2+H_2 = CO+H_2O$, RWGS). Catalysts with magnesium aluminum silicate as the support have a higher molar ratio of H_2/CO relatively, demonstrating their capabilities of inhibiting RWGS reaction.

The change of light-to-fuel efficiency η over time is shown in Fig. 3c, the average light-to-fuel efficiency η of Ni@SiO$_2$ is 11.6%. The reason is that when metal particles are directly exposed to the outer surface of SiO$_2$ without any restriction, metal particles tend to grow or aggregate, so that catalytic activities will be inhibited. The average light-to-fuel efficiency η of Ni/Al$_2$O$_3$@SiO$_2$ is 26.7%, and is lower than that of Ni/MgO@SiO$_2$ (η is 27.4%). The main problem lies in relatively poor stability of Ni/Al$_2$O$_3$@SiO$_2$, whose performance has an obvious decline with time compared with Ni/MgO@SiO$_2$. The average light-to-fuel efficiency η of Ni/Mg$_{0.67}$AlO$_x$@SiO$_2$ reaches 29.6%. As the molar ratio of Mg/Al increases, the light-to-fuel efficiency η further rises. The average light-to-fuel efficiency of Ni/Mg$_{1.22}$AlO$_x$@SiO$_2$ is 34.5%. Ni/Mg$_{1.78}$AlO$_x$@SiO$_2$ has the highest average light-to-fuel efficiency η of 35.7%. However, as the proportion of Mg^{2+} continues to increase, the performance begins to decline. The average light-to-fuel efficiency η of Ni/Mg$_{2.03}$AlO$_x$@SiO$_2$ is only 31.7%. In contrast to other strategies for solar thermochemical CO_2 reduction by CH$_4$ below 800 °C (Fig. 3d), Ni/Mg$_{1.78}$AlO$_x$@SiO$_2$ possesses a record-high light-to-fuel efficiency and its conversion of CH$_4$ is as high as 70.9% (Table 2), which is a significant advantage. Excellent photothermocatalytic durability is another advantage. After 24 h of reaction (Fig. 3e), it's r_{H_2} and r_{CO} values slightly decrease, and the η value remains as high as 34.6%. And the average size of Ni nanoparticles of used catalysts is 13.7 nm (Fig. 3f), which maintains a small size. Furthermore, there are no obvious carbon species on the catalyst. Other catalysts with molar ratios of Mg/Al of 1.22, 0.67 and 2.03 also show relatively better stability than those catalysts containing single metal support during experiment tests (Fig. S7). Another important reason why Ni/MgAlO$_x$@SiO$_2$ catalysts have different catalytic performances lies in different Ni nanoparticle sizes (Fig. S3). Basically, the smaller the metal size, the better activity and stability the catalyst exhibits.

3.3. Origin of carbon deposition inhibition

3.3.1. Carbon deposition properties

It is well known that carbon deposition properties have a heavy influence on catalyst activity [40,41], thus thermal gravimetric (TG) was employed (Fig. 4a and S7) to quantify the amount of carbon deposited during reactions. All spent catalysts show a significant weight loss in the range between 500 and 700 °C, due to the oxidation of these carbon species. These carbon species largely covering active sites severely damage catalysis performance. The amount of carbon deposited on the Ni/MgO@SiO$_2$ and Ni/Al$_2$O$_3$@SiO$_2$ are 45.57% and 42.05%, respectively. In contrast, the Ni/Mg$_{1.78}$AlO$_x$@SiO$_2$ catalyst displays the low-
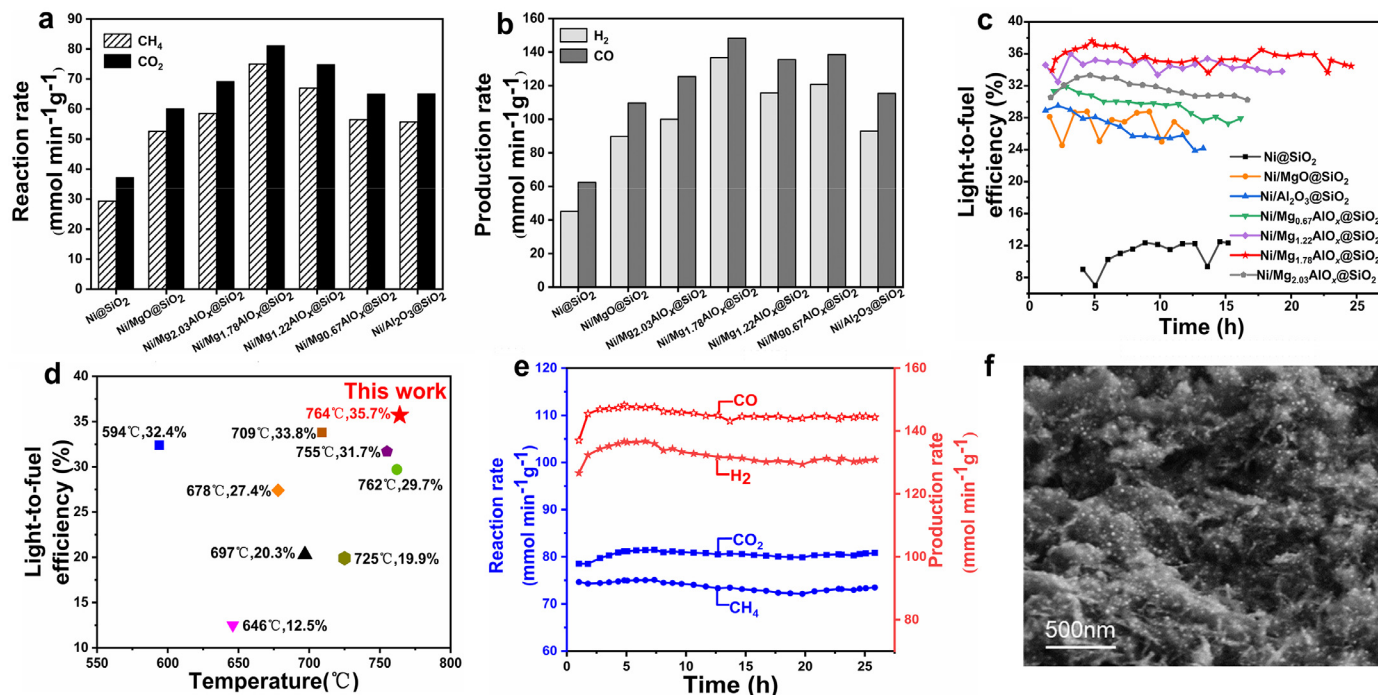
Fig. 3. Catalytic performance and light-to-fuel efficiency. (a) Reaction rates. (b) Production rates. (c) Light-to-fuel efficiency. (d) Comparison of light-to-fuel efficiency with literature included in Table 2. (e) Reaction and production rates for $Ni/Mg_{1.78}AlO_x@SiO_2$ under focused UV–vis-IR illumination and (f) SEM of $Ni/Mg_{1.78}AlO_x@SiO_2$ after photothermocatalytic reaction.

Table 2
Bibliographic listing of different types of catalysts and their performances in solar-driven CRM.

Catalyst	H_2/CO ratio	Conversion of CH_4 (%)	Reaction temperature (°C)	Light-to-fuel efficiency	Refs.
$SCM-Ni/SiO_2$	0.86	37.2	646	12.5%	[19]
$Ni/Ni-Al_2O_3$	0.94	34.3	725	19.9%	[24]
$Ni-La_2O_3/SiO_2$	0.89	48.5	697	20.3%	[38]
$Ni–CeO_2/SiO_2$	0.80	37.9	678	27.4%	[20]
$Ni_{1.6}Co/Co-Al_2O_3$	0.89	46.6	762	29.7%	[23]
$MCM-Ni/Ni-MgO$	0.88	40.9	755	31.7%	[25]
$NiCo-ZIF/Al2O3$	0.83	43.4	594	32.4%	[26]
$Ni/Mg-Al_2O_3$	0.93	38.6	703	32.9%	[39]
$Ni_1Co/AlMg-LDH$	0.85	54.1	709	33.8%	[21]
$Ni/Mg_{1.78}AlO_x@SiO_2$	0.92	70.9	764	35.7%	**This work**

est weight loss of 12.15%, suggesting that the quantity of active and graphitic carbon formed is minimal. $Ni/Mg_{1.78}AlO_x@SiO_2$ also has the lowest carbon deposition rate of 0.005 g_c g^{-1}_{cat} h^{-1} (Fig. 4b). XRD analysis shows that the deposited carbon exists in the form of graphite 2H (PDF 75–1621) in spent samples of $Ni/Mg_{1.78}AlO_x@SiO_2$ (Fig. S8). The carbon deposition rates of $Ni/Al_2O_3@SiO_2$ (r_c = 0.056 g_c g^{-1}_{cat} h^{-1}) and $Ni/MgO@SiO_2$ (r_c = 0.070 g_c g^{-1}_{cat} h^{-1}) are 11.2 times and 14 times as high as that of $Ni/Mg_{1.78}AlO_x@SiO_2$, respectively. The results indicate $Ni/MgAlO_x@SiO_2$ catalysts are good at inhibiting carbon deposition. According to Fig. 4c, carbon species type, active or graphitic, can be determined with the help of the Raman spectrum [42]. One peak at 1342 cm^{-1} could be assigned to D band, coming from active carbon, and the other at 1578 cm^{-1} could be assigned to G band, coming from graphitic carbon [43,44]. The D band is deemed to be the vibration of carbon atoms with dangling bonds in an amorphous carbon network while the G band is contributed by the C–C stretching vibrations of graphite layers [29,45]. The relative intensity of I_G/I_D could reflect the ratio of active carbon to graphite carbon [13,46] (Fig. 4d). The high I_G/I_D ratio of Ni @SiO_2, $Ni/MgO@SiO_2$ and $Ni/Al_2O_3@SiO_2$ confirmed that main carbon species are active carbon [13]. Activated carbon can cover more catalytic active sites, which is more harmful to the stability of the reaction compared with graphitic carbon. The

I_G/I_D of $Ni/MgAlO_x@SiO_2$ samples is lower, demonstrating the advantage of combining MgO and Al_2O_3 in enhancing stability. The I_G/I_D of $Ni/Mg_{1.78}AlO_x@SiO_2$ is 0.92, which is the lowest among all samples, agreeing with its excellent stability shown in Fig. 3c.

In most cases, CH_4 dissociation and CO disproportionation are generally sources of carbon deposition [21,38]. To investigate the main source, temperature-programmed CH_4 decomposition (TPMD) and CO disproportionation (TPCD) were conducted. As shown in Fig. S12, $Ni/MgAlO_x@SiO_2$ catalysts display a relatively stronger TCD signal with CH_4 decomposition rate rising, implying the formation of carbon deposition. CO disproportionation begins to occur above 300 °C (Fig. 4e). Notably, $Ni/MgO@SiO_2$ and $Ni/Al_2O_3@SiO_2$ show the strongest and weakest CO consumption peaks, respectively. This suggests that Al_2O_3 helps to inhibit the side reaction of CO disproportionation. Although peaking around 395 °C, TPCD signals of $Ni/MgAlO_x@SiO_2$ catalysts also have two relatively weak peaks around 450 °C and 550 °C. Around practical operation temperature of 700 to 800 °C, TPCD signals become weak since CO disproportionation itself is an exothermic reaction and will be inhibited at high temperature conditions. The carbon deposition amounts of TPMD and TPCD are determined by TG. Carbon deposition rates of TPMD are higher than that of TPCD for all samples (Fig. 4f), illustrating that methane cracking is the main source of carbon deposition.
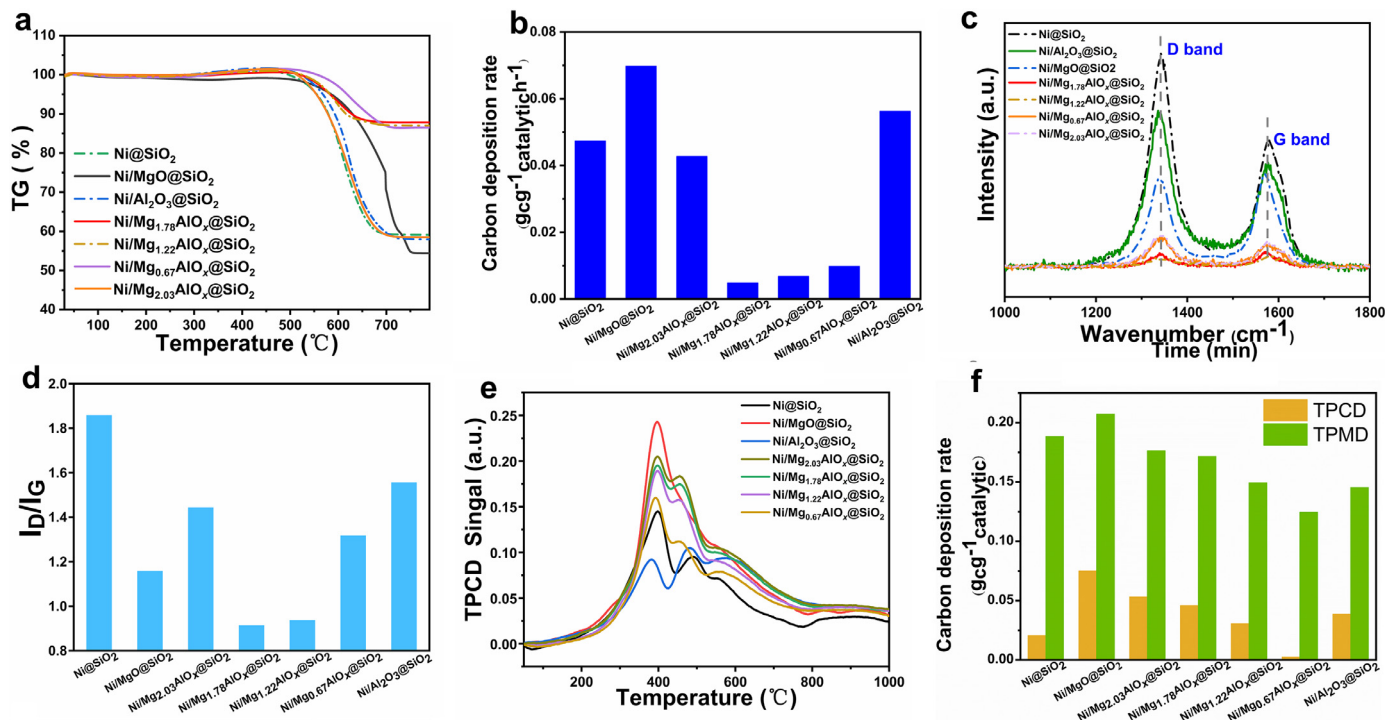
Fig. 4. Carbon deposition properties. (a) TG profiles of all used samples. (b) Carbon deposition rates. (c) Raman spectrum. (d) I_D/I_G ratios. (e) CO-TPCD profiles. (f) carbon deposition after TPMD and TPCD tests.

Note that the carbon deposition of $Ni/Mg_{1.78}AlO_x@SiO_2$ during TPCD or TPMD is not the lowest, but these carbon species can be quickly oxidized by CO_2. This is because $Ni/Mg_{1.78}AlO_x@SiO_2$ has a strong adsorption of CO_2 as confirmed by previous CO_2-TPD measurements (Fig. 2b). That explains why $Ni/Mg_{1.78}AlO_x@SiO_2$ has the lowest carbon deposition rate during practical operation tests (Fig. 4b).

3.3.2. Contribution of active oxygen in the support

To identify whether the lattice oxygen of $MgAlO_x@SiO_2$ contributes to inhibiting carbon deposition, an isotope labeling experiment using $^{12}C^{18}O_2$ and $^{12}CH_4$ was performed (Supplementary Information). The gas in the reactor cavity was injected into GC–MS for detection before turning on the lamp. Only three peaks can be observed corresponding to carrier gas (Ar), and reaction gas $^{12}CH_4$ and $C^{18}O_2$ (Fig. 5a). The retention time is located at 8.4–8.6 min corresponding to $^{12}CH_4$, and $m/z =$ 16.1, 15.1 and 14.1 belong to $^{12}CH_4$ and its fragments. The retention time of $C^{18}O_2$ is located at 11.4–12.0 min, $m/z =$ 48.1, 46.1, and 44 belong to $^{12}C^{18}O_2, ^{12}C^{18}O^{16}O$ and $^{12}C^{16}O_2$, respectively (Fig. 5b), indicating that the air in the reactor had been cleaned in advance. Then we turned on the Xe lamp for 2 h to introduce concentrated light irradiation. After that, the reacted gas was injected into GC–MS for measurement. The intensity of $m/z =$ 16.1, 15.1, 14.1(CH_4) and $m/z =$ 48.0 ($C^{18}O_2$) is weakened (Fig. 5b), and the additional crack peak at 7.6–7.8 min was attributed to CO (Fig. 5a). Corresponding intensities of fragments of $m/z =$ 28.1 ($^{12}C^{16}O$) and 30.1 ($^{12}C^{18}O$) significantly increased (Fig. 5b), illustrating that CRM reaction occurred. The fragment strength corresponding to $^{12}C^{18}O_2$ decreased, while the fragment strength corresponding to $^{12}C^{16}O_2$ and $^{12}C^{16}O^{18}O$ significantly increased. During the reaction, $^{12}C^{18}O_2$ is the only oxygen-containing reactant. As a result, the only source of ^{16}O is the catalyst, which comes from the lattice oxygen in $MgAlO_x@SiO_2$. This is beneficial to reducing carbon deposition and promoting a highly active and stable photothermocatalytic reaction.

3.3.3. DFT calculations

In order to understand the improvement of Ni nanocluster catalysts with different substrates, we modeled pyramidal NPs loaded on

slabs of $MgAl_2Si_2O_{10}H_4$, $Mg_3Si_4O_{12}H_2$ and $Al_2Si_2O_9H_4$. For comparison, Ni (111) surface models were also established. All substrates are constructed with $4 \times 2 \times 1$ supercell with the (001) facet cleaved. Ni NPs are built as a pyramid of exposed (111) surfaces with 30 atoms. Calculations are carried out in the framework of DFT using the generalized gradient approximation (GGA) of Perdew–Burke-Ernzerhof (PBE) [47]. The VASP (Vienna ab initio simulation package) package is employed with the projected augmented-wave method [48,49]. The kinetic cutoff energy for the plane-wave basis is set to 400 eV. The Brillouin zone integration was performed on a Gamma-centered $1 \times 1 \times 1$ K mesh. All the atoms are fully relaxed until the force on each atom is less than 0.05 eV /Å. To analyze the performance of catalysts, we used the periodic slab models with a vacuum layer of 15 Å. Our unit cell contained four layers with two bottom layers fixed to relax the module of the slab. Transition state searches were conducted using the climbing image nudged elastic band (CI-NEB) [50,51].

CH_4 and CO_2 are activated to form active species, which are the premise of CRM. The elementary steps of CRM reaction mainly include three parts: CH_4 activation dehydrogenation, CO_2 activation and oxidation of CH^* and C^* species. It is crucial for CRM reaction to oxidize CH^* or C^* species to remove the carbon deposition and suppress the deactivation of the catalyst. The reaction energy (ΔE) and activation energy (E_{act}) of the elementary steps of the DRM reaction are shown in Table S1. For simplifying the calculation, the E_{act} calculates several key steps in the reaction. The reaction energy diagram for CRM on Ni (111) surfaces is depicted in Fig. 5c. It can be seen that the E_{act} for CH_4 to remove an H atom to become CH_3^* on the surface of $Ni/Mg_{1.78}AlO_x@SiO_2$ is lower than that of other supports, which only needs 0.85 eV. This ensures a high reaction rate (entry 1 of Table S1) of CH_4 activation and is also consistent with our experimental results. Besides, from the perspective of reducing carbon deposition, the E_{act} value of CH^* oxidation to CHO^* (1.02 eV) is less than the E_{act} value of CH^* dissociation to C^* (1.22 eV) for $Ni/Mg_{1.78}AlO_x@SiO_2$ (Fig. S13). Subsequently, C^* species formation is suppressed. On the contrary, $Ni/Al_2O_3@SiO_2$ needs the highest energy to oxidize CH^* (1.44 eV), while the E_{act} value of CH^* dissociation is only 1.24 eV, which causes more carbon species deposition (Table S1).
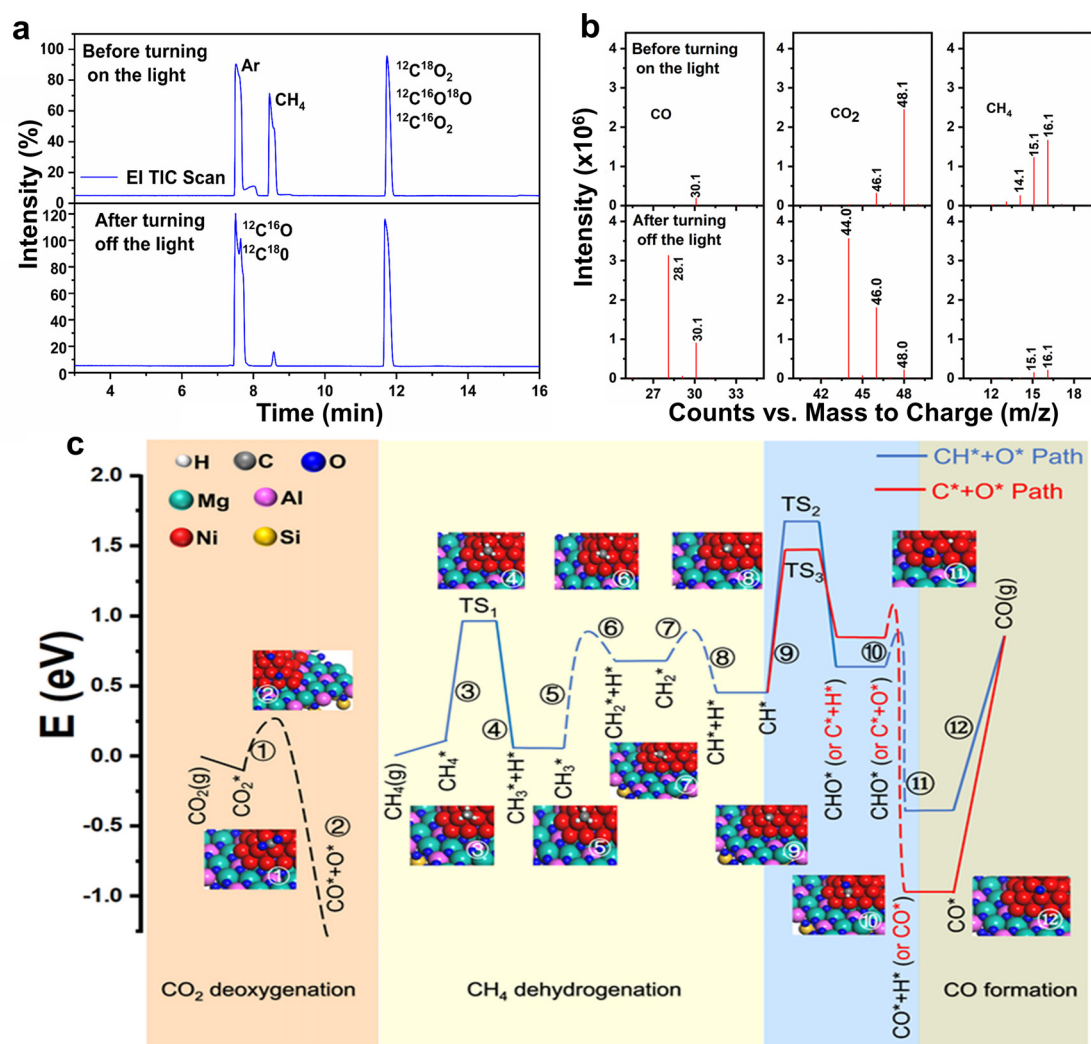
Fig. 5. Contribution of active oxygen and DFT calculation. (a) Gas chromatogram and (b) Mass spectrum of ^{18}O isotopic labeling experiment on Ni/Mg$_{1.78}$AlO$_x$@SiO$_2$ under focused UV–vis–IR illumination. (c)The reaction path of CRM on Ni/ Mg$_{1.78}$AlO$_x$@SiO$_2$ catalyst.

3.4. Decreased apparent activity energy under direct solar irradiation

It has been reported that Ni nanoparticles can simultaneously act as active sites and plasmonic promoters under light illumination [52–54]. Hence, distinct catalysis performances may be observed between light illumination and dark conditions. To reveal how the light affects the photothermocatalytic CRM reaction, optical absorption properties of Ni@SiO$_2$, Ni/MgO@SiO$_2$, Ni/Al$_2$O$_3$@SiO$_2$ and Ni/Mg$_{1.78}$AlO$_x$@SiO$_2$ were measured firstly (Fig. 6a). Since light excites surface plasmon resonances of Ni nanoparticles [55], all samples show good solar absorption properties. Although Ni/Mg$_{1.78}$AlO$_x$@SiO$_2$ has an intermediate absorptance compared with Ni/MgO@SiO$_2$ and Ni/Al$_2$O$_3$@SiO$_2$, its value is still over 80% across the entire solar spectra. To check whether high temperature plays a vital role in the solar-driven CRM, the experiment was conducted at near room temperature for Ni/Mg$_{1.78}$AlO$_x$@SiO$_2$. No H$_2$ or CO was detected (Fig. S14). This demonstrates that the high photothermocatalytic activity of Ni/MgAlO$_x$@SiO$_2$ is derived from light-driven thermocatalytic CRM.

To directly compare differences between photothermocatalysis and thermocatalysis, CRM reactions over Ni/Mg$_{1.78}$AlO$_x$@SiO$_2$ were performed under light irradiation and dark conditions. It can be seen from Fig. 6b that whether driven by light or heat, the reaction rate of the re-actants increases with temperature, indicating that high temperature is conducive to the catalytic reaction. At any temperature between 660 °C and 860 °C, the reaction activity of Ni/Mg$_{1.78}$AlO$_x$@SiO$_2$ under light irradiation is better than that in dark conditions. The ratio of H$_2$/CO under dark conditions is always lower than that of photothermocatalysis at the same temperature (Fig. 6c), although it increases with temperature for both cases since RWGS is inhibited by high-temperature conditions.

Kinetic studies are conducted to further explore how light irradiation affects solar CRM performances. Arrhenius plots using the conversion rate of CH$_4$ under both UV–vis-IR illumination and dark conditions are presented in Fig. 6d. These curves demonstrate a good linear relationship, and have a good agreement with the Arrhenius equation [26,56] ($k = Ae^{-E_a/RT}$). Accordingly, the apparent activation energy for CH$_4$ of Ni/Mg$_{1.78}$AlO$_x$@SiO$_2$ with focused UV–vis–IR irradiation is 31.2 kJ mol^{-1}, which is much less than that under dark conditions (70.3 kJ mol^{-1}). The decrease in apparent activation energy can be ascribed to the excitation of hot electrons in metallic Ni. It has been demonstrated by several references that excited Ni can dramatically decrease the activation energy of CO$_2$ dissociation and CH* oxidation compared with ground states (dark conditions) [16,19,20,52]. This explains the reduced apparent activation energy and promoted activity of Ni/Mg$_{1.78}$AlO$_x$@SiO$_2$ under direct light illumination.

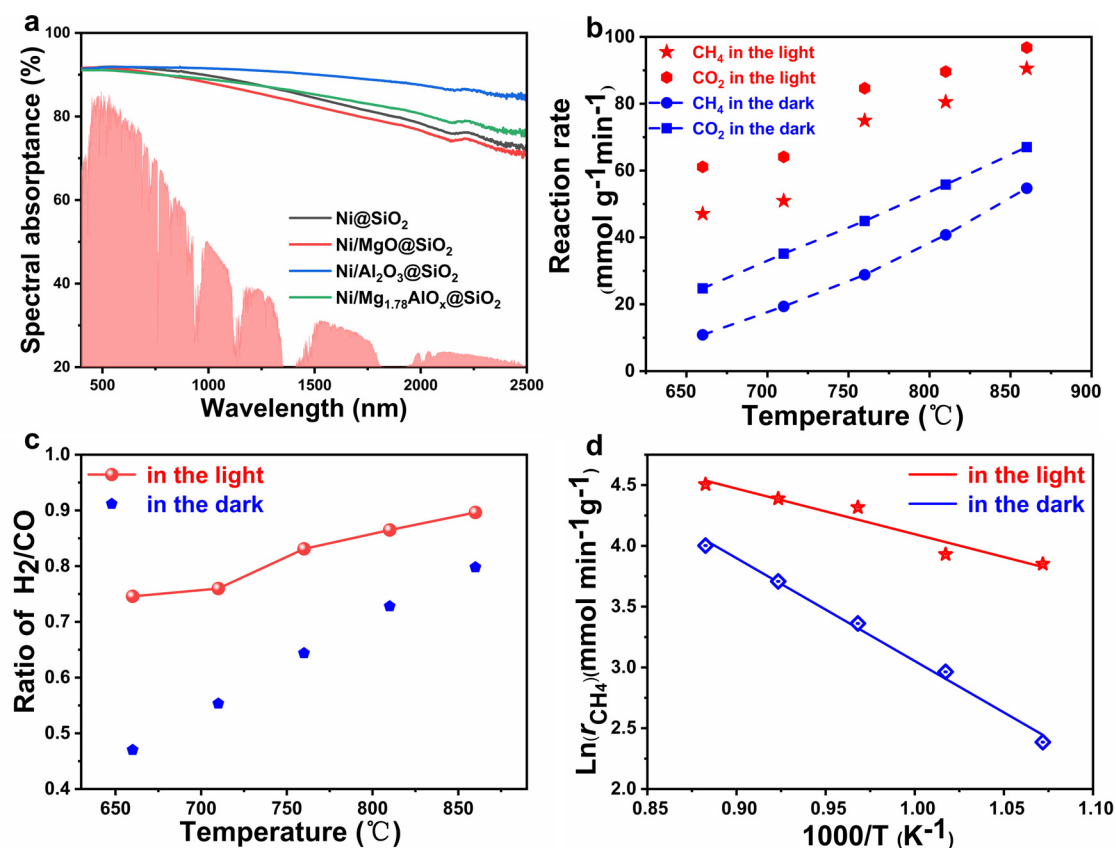**Fig. 6. Performance comparison for CRM and reaction kinetics.** (a) Absorption spectra of Ni@SiO$_2$, Ni/MgO@SiO2, Ni/Al$_2$O$_3$@SiO$_2$, Ni/Mg$_{1.78}$AlO$_x$@SiO$_2$. (b) CH$_4$ and CO$_2$ reaction rates at different temperatures. (c) Molar ratios of H$_2$/CO and (d) Arrhenius plot in terms of reaction rates of CH$_4$ for CRM on Ni/Mg$_{1.78}$AlO$_x$@SiO$_2$ under dark and focused irradiation conditions.

4. Conclusion

In summary, highly efficient solar-driven CO$_2$ conversion with CH$_4$ is achieved via interconnected Ni/MgAlO$_x$ nanoflakes grown on SiO$_2$ particles with an ultrahigh light-to-fuel efficiency of 35.7% below 800 ℃. The excellent performance can be ascribed to the following three aspects. First of all, highly dispersed nickel nanoparticles with small sizes and strong metal-support interactions are realized on Ni/MgAlO$_x$@SiO$_2$. And the formation of Mg-Al phyllosilicate provides many basic sites, promoting the absorption and activation of CO$_2$ molecules. Secondly, the active oxygen in the carrier participates in the solar-driven CRM reaction, which is beneficial to suppressing the formation of carbon species produced by CH$_4$ dissociation and CO disproportionation. DFT calculations also demonstrate that the reaction on MgAlO$_x$@SiO$_2$ has a lower activation energy of CH* oxidation to CHO* and improves the dissociation of CH$_4$ to CH$_3$*. At last, full-spectrum solar energy can be efficiently captured and the light-driven CRM greatly reduces the apparent activation energy, thereby significantly improving catalytic activities under direct light illumination. Our work demonstrates that Ni/MgAlO$_x$@SiO$_2$ can realize solar-driven CO$_2$ conversion with ultrahigh light-to-fuel efficiency and superior stability, thus is promising to provide new opportunities for tackling global climate change and energy shortage problems.

Declaration of competing interest

The authors declare no conflicts of interest in this work.

Acknowledgments

Supplementary materials

Supplementary material associated with this article can be found, in the online version, at doi:10.1016/j.fmre.2022.04.011.

References

[1] D. Touma, S. Stevenson, F. Lehner, et al., Human-driven greenhouse gas and aerosol emissions cause distinct regional impacts on extreme fire weather, Nat. Commun. 12 (2021) 212.

[2] S.J.A. Moniz, S.A. Shevlin, D.J. Martin, et al., Visible-light driven heterojunction photocatalysts for water splitting – a critical review, Energy Environ. Sci. 8 (2015) 731–759.

[3] M. Asadi, M.H. Motevaselian, A. Moradzadeh, et al., Highly efficient solar-driven carbon dioxide reduction on molybdenum disulfide catalyst using choline chloride-based electrolyte, Adv. Energy Mater. 9 (2019) 1803536.

[4] S. Yu, P.K. Jain, Plasmonic photosynthesis of C$_1$-C$_3$ hydrocarbons from carbon dioxide assisted by an ionic liquid, Nat. Commun. 10 (2019) 2022.

[5] G. Zhang, J. Liu, J. Li, et al., Radiocarbon isotope technique as a powerful tool in tracking anthropogenic emissions of carbonaceous air pollutants and greenhouse gases: A review, Fundam. Res. 1 (2021) 306–316.

[6] J. Chang, P. Ciais, T. Gasser, et al., Climate warming from managed grasslands cancels the cooling effect of carbon sinks in sparsely grazed and natural grasslands, Nat. Commun. 12 (2021) 118.

[7] Y. Zhang, S. Kang, D. Wei, et al., Sink or source? Methane and carbon dioxide emissions from cryoconite holes, subglacial sediments, and proglacial river runoff during intensive glacier melting on the Tibetan Plateau, Fundam. Res. 1 (2021) 232–239.

[8] Y.R. Wang, R.X. Yang, Y. Chen, et al., Chloroplast-like porous bismuth-based core–shell structure for high energy efficiency CO$_2$ electroreduction, Sci. Bull. 65 (2020) 1635–1642.

[9] K. Gao, X. Liu, T. Wang, et al., Sr-doped SmMnO$_3$ perovskites for high-performance near-isothermal solar thermochemical CO$_2$-to-fuel conversion, Sustain. Energy Fuels 5 (2021) 4295–4310.

[10] Z. Qin, J. Chen, X. Xie, et al., CO_2 reforming of CH_4 to syngas over nickel-based catalysts, Environ. Chem. Lett. 18 (2020) 997–1017.

[11] V. Danghyan, A. Kumar, A. Mukasyan, et al., An active and stable NiOMgO solid solution based catalysts prepared by paper assisted combustion synthesis for the dry reforming of methane, Appl. Catal. B Environ. 273 (2020) 119056.

[12] H.A. Lara-García, D.G. Araiza, M. Méndez-Galván, et al., Dry reforming of methane over nickel supported on Nd–ceria: Enhancement of the catalytic properties and coke resistance, RSC Adv. 10 (2020) 33059–33070.

[13] D. Guo, Y. Lu, Y. Ruan, et al., Effects of extrinsic defects originating from the interfacial reaction of CeO_2-x-nickel silicate on catalytic performance in methane dry reforming, Appl. Catal. B Environ. 277 (2020) 119278.

[14] M. Liu, Y.-.R. Wang, H.-.M. Ding, et al., Self-assembly of anthraquinone covalent organic frameworks as 1D superstructures for highly efficient CO_2 electroreduction to CH_4, Sci. Bull. 66 (2021) 1659–1668.

[15] J.W. Wang, L. Jiang, H.H. Huang, et al., Rapid electron transfer via dynamic coordinative interaction boosts quantum efficiency for photocatalytic CO_2 reduction, Nat. Commun. 12 (2021) 4276.

[16] L. Zhou, J.M.P. Martirez, J. Finzel, et al., Light-driven methane dry reforming with single atomic site antenna-reactor plasmonic photocatalysts, Nat. Energy 5 (2020) 61–70.

[17] J. Chen, C. Dong, H. Idriss, et al., Metal halide perovskites for solar-to-chemical fuel conversion, Adv. Energy Mater. 10 (2019) 1902433.

[18] L. Liu, H. Huang, F. Chen, et al., Cooperation of oxygen vacancies and 2D ultrathin structure promoting CO_2 photoreduction performance of $Bi_4Ti_3O_{12}$, Sci. Bull. 65 (2020) 934–943.

[19] H. Huang, M. Mao, Q. Zhang, et al., Solar-light-driven CO_2 reduction by CH_4 on silica-cluster-modified ni nanocrystals with a high solar-to-fuel efficiency and excellent durability, Adv. Energy Mater. 8 (2018) 1702472.

[20] Z. Jiang, Y. Li, Q. Zhang, et al., A novel nanocomposite of mesoporous silica supported Ni nanocrystals modified by ceria clusters with extremely high light-to-fuel efficiency for UV-vis-IR light-driven CO_2 reduction, J. Mater. Chem. A 7 (2019) 4881–4892.

[21] X. Liu, H. Shi, X. Meng, et al., Solar-enhanced CO_2 conversion with CH_4 over synergetic NiCo alloy catalysts with light-to-fuel efficiency of 33.8%, Sol. RRL 5 (2021) 2170085.

[22] D. Marxer, P. Furler, M. Takacs, et al., Solar thermochemical splitting of CO_2 into separate streams of CO and O_2 with high selectivity, stability, conversion, and efficiency, Energy Environ. Sci. 10 (2017) 1142–1149.

[23] S. Wu, Y. Li, Q. Zhang, et al., Formation of NiCo alloy nanoparticles on Co doped Al_2O_3 leads to high fuel production rate, large light-to-fuel efficiency, and excellent durability for photothermocatalytic CO_2 reduction, Adv. Energy Mater. 10 (2020) 2002602.

[24] Q. Zhang, Y. Li, S. Wu, et al., UV-vis-IR irradiation driven CO_2 reduction with high light-to-fuel efficiency on a unique nanocomposite of Ni nanoparticles loaded on Ni doped Al_2O_3 nanosheets, J. Mater. Chem. A 7 (2019) 19800–19810.

[25] S. Wu, Q. Hu, Y. Li, Photothermocatalytic CO_2 reduction on magnesium oxide-cluster-modified Ni nanoparticles with high fuel production rate, large light-to-fuel efficiency and excellent durability, Sol. RRL 5 (2021) 2100735.

[26] X. Liu, Z. Mu, C. Sun, et al., Highly efficient solar-driven CO_2-to-fuel conversion assisted by CH_4 over NiCo-ZIF derived catalysts, Fuel 310 (2021) 122441.

[27] Q. Zhang, X. Feng, J. Liu, et al., Hollow hierarchical Ni/MgO-SiO_2 catalyst with high activity, thermal stability and coking resistance for catalytic dry reforming of methane, Int. J. Hydrog. Energy 43 (2018) 11056–11068.

[28] D. Chen, K. Christensen, E. Ochoafernandez, et al., Synthesis of carbon nanofibers: Effects of Ni crystal size during methane decomposition, J. Catal. 229 (2005) 82–96.

[29] K. Han, W. Yu, L. Xu, et al., Reducing carbon deposition and enhancing reaction stability by ceria for methane dry reforming over Ni@SiO_2@CeO_2 catalyst, Fuel 291 (2021) 120182.

[30] H. Peng, X. Zhang, L. Zhang, et al., One-pot facile fabrication of multiple nickel nanoparticles confined in microporous silica giving a multiple-cores@shell structure as a highly efficient catalyst for methane dry reforming, ChemCatChem 9 (2017) 127–136.

[31] D. Esrafilzadeh, A. Zavabeti, R. Jalili, et al., Room temperature CO_2 reduction to solid carbon species on liquid metals featuring atomically thin ceria interfaces, Nat. Commun. 10 (2019) 865.

[32] K. Sheng, D. Luan, H. Jiang, et al., Ni_xCo_y nanocatalyst Supported by ZrO_2 hollow sphere for dry reforming of methane: Synergetic catalysis by Ni and Co in alloy, ACS Appl. Mater. Interfaces 11 (2019) 24078–24087.

[33] Z. Taherian, A. Khataee, Y. Orooji, Nickel-based nanocatalysts promoted over MgO–modified SBA-16 for dry reforming of methane for syngas production: Impact of support and promoters, J. Energy Inst. 97 (2021) 100–108.

[34] X. Wang, X. Bai, Y. Guo, et al., A nanoscale Ni/ZrO_2 catalyst coated with Al_2O_3 for carbon dioxide reforming of methane, J. Chem. Technol. Biotechnol. 96 (2021) 474–480.

[35] Q. Wei, X. Gao, G. Liu, et al., Facile one-step synthesis of mesoporous Ni-Mg-Al catalyst for syngas production using coupled methane reforming process, Fuel 211 (2018) 1–10.

[36] J. Chen, L. Duan, F. Donat, et al., Assessment of the effect of process conditions and material characteristics of alkali metal salt promoted MgO-based sorbents on their CO_2 capture performance, ACS Sustain. Chem. Eng. 9 (2021) 6659–6672.

[37] X. Du, D. Zhang, R. Gao, et al., Design of modular catalysts derived from NiMgAl-LDH@m-SiO_2 with dual confinement effects for dry reforming of methane, Chem. Commun. 49 (2013) 6770–6772.

[38] G. Zhang, S. Wu, Y. Li, et al., Significant improvement in activity, durability, and light-to-fuel efficiency of Ni nanoparticles by La_2O_3 cluster modification for photothermocatalytic CO_2 reduction, Appl. Catal. B Environ. 264 (2020) 118544.

[39] X. Tan, S. Wu, Y. Li, et al., Highly efficient photothermocatalytic CO_2 reduction in Ni/Mg-doped Al_2O_3 with high fuel production rate, large light-to-fuel efficiency, and good durability, Energy Environ. Mater. 0 (2021) 1–10.

[40] X. Zhang, C. Yang, Y. Zhang, et al., Ni–Co catalyst derived from layered double hydroxides for dry reforming of methane, Int. J. Hydrog. Energy 40 (2015) 16115–16126.

[41] S. Damyanova, B. Pawelec, K. Arishtirova, et al., Ni-based catalysts for reforming of methane with CO_2, Int. J. Hydrog. Energy 37 (2012) 15966–15975.

[42] D.C. Upham, V. Agarwal, A. Khechfe, et al., Catalytic molten metals for the direct conversion of methane to hydrogen and separable carbon, Science 358 (2017) 917–921.

[43] X. Zhao, H. Li, J. Zhang, et al., Design and synthesis of NiCe@m-SiO_2 yolk-shell framework catalysts with improved coke- and sintering-resistance in dry reforming of methane, Int. J. Hydrog. Energy 41 (2016) 2447–2456.

[44] F. Wang, Y. Wang, L. Zhang, et al., Performance enhancement of methane dry reforming reaction for syngas production over $Ir/Ce_{0.9}La_{0.1}O_2$-nanorods catalysts, Catal. Today 355 (2020) 502–511.

[45] C. Palmer, D.C. Upham, S. Smart, et al., Dry reforming of methane catalysed by molten metal alloys, Nat. Catal. 3 (2020) 83–89.

[46] Z.-.Y. Lim, J. Tu, Y. Xu, et al., Enhanced porosity of Ni@Hollow meso-SiO_2 catalyst for CO_2 reforming of methane, Int. J. Hydrog. Energy 46 (2021) 7866–7877.

[47] P. John, Perdew, et al., Generalized gradient approximation made simple, Phys. Rev. Lett. 77 (1997) 3865.

[48] P.E. Blochl, Projector augmented-wave method, Phys. Rev. B Condens. Matter 50 (1994) 17953–17979.

[49] G. Kresse, D. Joubert, From ultrasoft pseudopotentials to the projector augmented-wave method, Phys. Rev. B 59 (1999) 1758–1775.

[50] D. Sheppard, P. Xiao, W. Chemelewski, et al., A generalized solid-state nudged elastic band method, J. Chem. Phys. 136 (2012) 074103.

[51] G. Henkelman, B.P. Uberuaga, H. Jónsson, A climbing image nudged elastic band method for finding saddle points and minimum energy paths, J. Chem. Phys. 113 (2000) 9901–9904.

[52] H. Liu, H. Song, X. Meng, et al., Light irradiation enhanced CO_2 reduction with methane: A case study in size-dependent optical property of Ni nanoparticles, Catal. Today 335 (2019) 187–192.

[53] H. Liu, T.D. Dao, L. Liu, et al., Light assisted CO_2 reduction with methane over group VIII metals: Universality of metal localized surface plasmon resonance in reactant activation, Appl. Catal. B Environ. 209 (2017) 183–189.

[54] C. Wang, Y. Su, A. Tavasoli, et al., Recent advances in nanostructured catalysts for photo-assisted dry reforming of methane, Mater. Today Nano 14 (2021) 100113.

[55] S. Wu, S. Wu, Y. Sun, Light-driven dry reforming of methane on metal catalysts, Sol. RRL 5 (2020) 2000507.

[56] Y. Tang, Y. Wei, Z. Wang, et al., Synergy of single-atom Ni_1 and Ru_1 sites on CeO_2 for dry reforming of CH_4, J. Am. Chem. Soc. 141 (2019) 7283–7293.

Xianglei Liu (BRID: 05908.00.98836) received his B.S. degree in Engineering from Xi'an Jiaotong University in 2011, and his Ph.D. degree in Mechanical Engineering from Georgia Institute of Technology in 2016. Since 2016, he has been a professor at the School of Energy and Power, Nanjing University of Aeronautics and Astronautics. His-research interests include micro-nano-scale heat transfer principles and applications, solar fuels, and thermal energy storage.

Yimin Xuan (BRID: 08830.00.60921) is a professor at the School of Energy and Power, Nanjing University of Aeronautics and Astronautics, China. He obtained his Ph.D. degree from the Institute of Thermodynamics at the National Defense University of Hamburg, Germany in 1991. He was elected as an academician of the Chinese Academy of Sciences in 2015. His-research interests mainly focus on solar energy harvesting, thermal management, and energy system analysis.